CHEMISTRY OF MATERIALS
Cite This: Chem. Mater. 2019, 31, 5993−6000
Article
pubs.acs.org/cm

Multiferroism Induced by Spontaneous Structural Ordering in Antiferromagnetic Iron Perovskites

Xabier Martínez de Irujo-Labalde,[†] Masato Goto,[‡] Esteban Urones-Garrote,[†] Ulises Amador,[§] Clemens Ritter,[∥] Midori E. Amano Patino,[‡] Anucha Koedtruad,[‡] Zhenhong Tan,[‡] Yuichi Shimakawa,[‡] and Susana García-Martín*[,†]

[†]Departamento de Química Inorgánica I, Facultad de Ciencias Químicas, Universidad Complutense, Madrid 28040, Spain
[‡]Institute for Chemical Research, Kyoto University, Uji, Kyoto 611-0011, Japan
[§]Facultad de Farmacia, Departamento de Química y Bioquímica, Universidad San Pablo-CEU, CEU Universities, Urbanización Montepríncipe, Boadilla del Monte, Madrid E-28668, Spain
[∥]Institut Laue-Langevin, 71 avenue des Martyrs, 38042Grenoble Cedex 9, France

Supporting Information

ABSTRACT: Room-temperature multiferroism in polycrystalline antiferromagnetic Fe perovskites is reported for the first time. In the perovskite-type oxides $RE_{1.2}Ba_{1.2}Ca_{0.6}Fe_3O_8$ (RE = Gd, Tb), the interplay of layered ordering of Gd(Tb), Ba, and Ca atoms with the ordering of FeO_4-tetrahedra (T) and FeO_6-octahedra (O) results in a polar crystal structure. The layered structure consists of the stacking sequence of RE/Ca-RE/Ca-Ba-RE/Ca layers in combination with the TOOT sequence in a unit cell. A polar moment of 33.0 $\mu C/cm^2$ for the Gd-oxide (23.2 $\mu C/cm^2$ for the Tb one) is determined from the displacements of the cations, mainly Fe, and oxygen atoms along the *b*-axis. These oxides present antiferromagnetic ordering doubling the *c*-axis, and the magnetic structure in the Tb-compound remains up to 690 K, which is one of the highest transition temperatures reported in Fe perovskites.

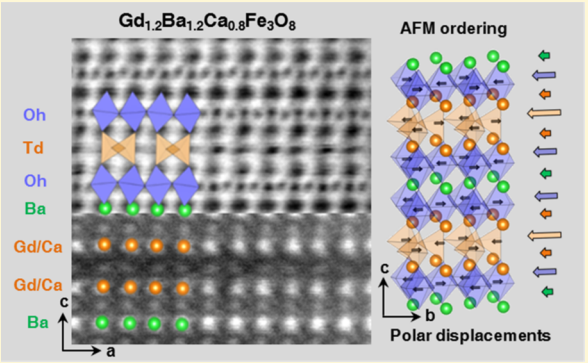

INTRODUCTION

The interplay between compositional diversity and rich defect-chemistry within the ABX_3 perovskite structure designates it as a versatile framework to reach a wide array of functional properties.[1] Perovskites are among the most important families of complex oxides. Transition metal atoms usually occupy the B-positions of the structure, whereas alkaline, alkaline-earth, and lanthanide atoms locate within the A-sites. Partial or total substitution of different A and B cations is a common strategy to modify and tune the properties of perovskite oxides. In addition to the compositional flexibility, the perovskite structure presents structural flexibility to accommodate the different sizes and oxidation states of the A and B cations. Tilting of the octahedral network formed by the anion sublattice is the most frequent distortion for optimizing the matching between the A−O and B−O bond distances.[2−4] This apparently simple distortion highly impacts the bandwidth of the electronic structure and consequently determines the conducting and magnetic properties of the oxide.[5] Also, the perovskite structure presents an outstanding ability to accommodate nonstoichiometry in the anion sublattice by creating anion vacancies. High concentration of anion vacancies originates different coordination polyhedra around the B-cations in addition to the BO_6 octahedra. Besides, cation ordering of different atoms sharing the same A or B sites gives different superstructures based on the perovskite-type,[6] having astonishing influence on the properties of the "ordered compounds" compared to the disordered ones.[7,8] Therefore, by a thorough selection of the type of atoms in both the A and B sites of the structure, a wide combination of ordering effects and properties is opened in the perovskite oxides. For instance, the interplay between cation ordering, oxygen vacancy ordering, and oxidation states of Cu determines the superconducting behavior in $YBa_2Cu_3O_{7-\delta}$;[9] the location of the anion vacancies within the (GdO)-planes of the layered perovskite $GdBaCo_2O_{5+\delta}$ plays an essential role in the conducting properties of this compound,[10] and the combination of cation ordering with the oxygen vacancy and charge orderings in $REBaMn_2O_{5.75}$ (RE = Gd, Tb) determines its transport and magnetic properties.[11,12]

Materials or systems with coexistence of properties for achieving multifunctionality are extremely attractive. In this context, magnetoelectric multiferroic materials, which present the coexistence of magnetic ordering and ferroelectricity, are

Received: July 9, 2019
Revised: July 16, 2019
Published: July 17, 2019

DOI: 10.1021/acs.chemmater.9b02716
Chem. Mater. 2019, 31, 5993−6000

among the most interesting from both academic point of view and applications.[13] In the case of perovskites, multiferroic behavior is not a trivial achievement because these two properties seem to conceptually exclude one another.[14] Despite this, there are ways to combine magnetism and ferroelectricity in perovskites such as $BiFeO_3$, in which magnetic ordering is associated with Fe, but the Bi lone-pair is responsible for the ferroelectric behavior.[15] Although ferromagnetism is usually the type of magnetic ordering occurring in magnetoelectric−multiferroic perovskites, the combination of ferroelectricity and antiferromagnetism has been predicted in the orthorhombic $BaMnO_3$[16] and in $YCaFe_2O_5F$.[17] Layered-type ordering of different A-cations coupled with particular octahedral tilting systems of the anion sublattice results in non-centrosymmetric polar perovskites.[18,19] A more recent approach consisting of the combination of cation ordering with anion-vacancy ordering to generate polar structures has been demonstrated on epitaxially grown $SrFeO_{2.5}/CaFeO_{2.5}$ thin-film superlattices.[20] The variety of coordination polyhedra that Fe can adopt makes this element ideal to promote coupling of cation and anion-vacancy orderings to form perovskite-based superstructures with different stoichiometries. Besides, stabilization of Fe^{3+} within the structure can provide strong superexchange interactions to sustain magnetic ordering above room temperature, as for instance in $YBaFe_2O_5$,[21] $YFeO_3$,[22] and $LaCa_2Fe_3O_8$.[23] The combination of these properties of iron can result in multiferroism, as it has been recently suggested for the layered perovskite $YCaFe_2O_5F$.[17] First-principle density functional theory calculations support strong polarization and robust magnetic ordering above room temperature in $YCaFe_2O_5F$; besides, the possibility of preparing this material by a layer-by-layer growth technique capable of imposing Y and Ca ordering has been suggested.

Taking into account these aspects, we report, in this article, the synthesis and characterization of the new room-temperature multiferroic oxides $RE_{1.2}Ba_{1.2}Ca_{0.6}Fe_3O_8$ (RE = Gd, Tb) with a perovskite-based crystal structure. These polycrystalline oxides present spontaneous layered ordering of Gd(Tb), Ba, and Ca atoms, which induces FeO_4-tetrahedra and FeO_6-octahedra ordering in a polar crystal structure. The crystal structure has been solved by means of advanced transmission electron microscopy (TEM) techniques with atomic resolution. These oxides present antiferromagnetic (AFM) ordering of Fe^{3+} up to 850 K, also showing both electric and magnetic phase transitions at the same temperature.

Experimental Methods. The initial composition of the compound to be subject of this study was $Gd_{0.8}Ba_{0.8}Ca_{0.4}Fe_2O_{5+\delta}$, as part of the system $Gd_{0.8}Ba_{0.8}Ca_{0.4}Co_{2-x}Fe_xO_{5+\delta}$. $Gd_{0.8}Ba_{0.8}Ca_{0.4}Fe_2O_{5+\delta}$ was synthesized by the ceramic route using Gd_2O_3 (Sigma-Aldrich, 99.99%), $BaCO_3$ (Sigma-Aldrich, 99.99%), $CaCO_3$ (Merck, 99.7%), and Fe_2O_3 (Sigma-Aldrich, 99.99%). Gd_2O_3 was heated at 1173 K prior to weighing in order to avoid $Gd(OH)_2$ contamination. Stoichiometric amounts of the starting materials were mixed and heated at 1173 K in air to decompose the carbonates. The sample was then pelletized and treated at 1473 K for 12 h with heating and cooling rates of 5 and 3 K min^{-1}, respectively. Subsequent cycles of regrinding and firing were performed in order to obtain single-phase samples. The isostructural oxide $Tb_{0.8}Ba_{0.8}Ca_{0.4}Fe_2O_{5+\delta}$ was prepared using the same ceramic method as used for the Gd-compound with the aim of performing neutron diffraction experiments, avoiding the strong neutron absorption of natural Gd.

The initial phase identification was carried out by powder X-ray diffraction (PXRD) using the PANalytical X'PERT PRO MPD diffractometer with the Cu Kα_1 radiation (λ = 1.5406 Å) and X'PERT PEAPS software. The pattern was taken in the step mode with a step size of 0.017 (2θ degrees) and an acquisition time per step of 10 s. The average structure of the material was studied by synchrotron X-ray diffraction (SXRD) at the beamline BL02B2 of Spring-8 (Hyogo, Japan). A scan at 300 K was performed using radiation of 0.599748 Å wavelength. The crystal structure parameters were refined by the Rietveld method using FullProf.[24] Besides, SXRD patterns at different temperatures were taken in air between 300 and 1050 K using a wavelength of 0.826560 Å at TPS (Taiwan Photon Source) beamline 09A in NSRRC (National Synchrotron Radiation Research Center) in Hsinchu, Taiwan. A LeBail fitting (without a structural model) of the SXRD patterns was performed to obtain the lattice parameters at different temperatures.

Thermogravimetric analysis (TGA) was carried out in order to evaluate the oxygen stoichiometry of the compound from 300 to 1173 K with heating and cooling rates of 5 K/min.

The nuclear and magnetic structures of the oxide $Tb_{0.8}Ba_{0.8}Ca_{0.4}Fe_2O_{5+\delta}$ were determined by neutron powder diffraction (NPD) on the D2B and D20 instruments at the ILL (Grenoble, France). High-resolution diffraction patterns were collected on D2B at 300 and 1000 K using a wavelength λ = 1.594 Å. To determine the thermal evolution of the magnetic structure, patterns were collected between 300 and 1000 K every 3.5 K on D20 with neutrons of λ = 2.41 Å by using a quartz tube open to air inside a furnace under vacuum. The data were fitted using FullProf.[24] Magnetic symmetry analysis was done using the program BASIREPS.[25,26]

High-resolution transmission electron microscopy (HRTEM), selected area electron diffraction (SAED), and electron energy loss spectroscopy (EELS) were performed with a JEOL JEM 3000F microscope operating at 300 kV (double tilt ±20°) fitted with a X-ray energy-dispersive spectroscopy (XEDS) microanalysis system (OXFORD INCA) and an ENFINA spectrometer with an energy resolution of 1.2 eV. The atomic ratio of the metals of the oxide was determined by XEDS analyses, showing good agreement between analytical and nominal composition in all crystals. The average oxidation state of Fe cations was determined by EELS. The spectra were acquired in the diffraction mode, with a dispersion of 0.1 eV/channel, a collection angle of $\beta \approx 5.4$ mrad, and an acquisition time of 1.5 s. A power-law model was used to remove the background of the spectra.

High-angle annular dark field (HAADF) and annular bright field (ABF) analyses were performed on an ARM200cF microscope fitted with a condenser lens aberration corrector [point resolution in the scanning transmission electron microscopy (STEM) mode of 0.08 nm]. HAADF images were acquired with an inner acceptance angle of 90 mrad and ABF ones with a collection angle of 11 mrad. The same ARM200cF microscope was employed for EELS experiments as it is fitted with a GIF Quantum-ER spectrometer. EELS mapping was performed with a collection semiangle $\beta \approx 30$ mrad, dispersion energy of 0.5 eV/channel, and collection time for each spectrum of 0.09 seconds. Gd-$M_{4,5}$, Fe-$L_{2,3}$, Ba-$M_{4,5}$, and Ca-$L_{2,3}$ edge signals were chosen for mapping.

DOI: 10.1021/acs.chemmater.9b02716
Chem. Mater. 2019, 31, 5993−6000

^{57}Fe Mössbauer spectra were measured to confirm the oxidation states and oxygen environments for the Fe cations and to study the magnetic states in the compound. The measurements were performed at room temperature in transmission geometry with a constant acceleration spectrometer using a ^{57}Co/Rh radiation source. The velocity scale and the isomer shift (IS) were determined with the relative values of α-Fe at room temperature. The spectrum was fitted to Lorentzian functions by using the standard least-squares method.

The magnetic properties of the compounds were measured by a CS-3 furnace apparatus at 5 Oe in the temperature ranging between 300 and 950 K.

Electrical conductivity was determined by a dc four-probe method on rectangular bars in the range between 300 and 1200 K by using a potentiostat/galvanostat equipment (Autolab PGSTAT302N) in the galvanostatic mode.

RESULTS AND DISCUSSION

Structural Characterization. The initial composition of one of the compounds to be subject of this study was $Gd_{0.8}Ba_{0.8}Ca_{0.4}Fe_2O_{5+\delta}$ as part of the system $Gd_{0.8}Ba_{0.8}Ca_{0.4}Co_{2-x}Fe_xO_{5+\delta}$. The PXRD pattern of the sample with composition $Gd_{0.8}Ba_{0.8}Ca_{0.4}Fe_2O_{5+\delta}$ is characteristic of a single-phase material with a perovskite-related structure (Supporting Information, Figure S1). A weak low-angle reflection appears at $2\theta \approx 7.5°$, which corresponds to an interplanar distance $d_{hkl} \approx 11.3$ Å, reflecting, in principle, a threefold superstructure. The average oxidation state of Fe in the present compound, close to 3+ (2.91 ± 0.04), has been determined from the L_3/L_2 intensity ratio of the Fe-$L_{2,3}$ ionization edge of several EELS spectra (Supporting Information, Figure S2). Taking into account this oxidation state of Fe found by EELS and that the XEDS analysis confirmed the nominal cation composition of the oxide, one can determine the oxygen content to $\delta = 0.33$, which agrees with the stoichiometric formula $Gd_{1.2}Ba_{1.2}Ca_{0.6}Fe_3O_8$.

Further investigations of the crystal structure were performed by SAED and HRTEM analyses. Figure 1 shows the SAED patterns along different zone axes of a crystal of the compound. All patterns have been indexed according to the cubic perovskite structure. The pattern along the $[001]_p$ zone axis shows the characteristic reflections of the cubic perovskite and weak extra reflections at $G_p \pm 1/2\ (110)_p^*$ associated with the formation of the so-called diagonal cell $(\sqrt{2}a_p \times \sqrt{2}b_p)$ within the ab plane. Moreover, in the SAED pattern along the $[010]_p$ zone axis, strong extra reflections at $G_p \pm 1/3\ (001)_p^*$ appear, revealing the threefold superstructure along the stacking axis. Both types of the abovementioned extra reflections at $G_p \pm 1/2\ (110)_p^*$ and $G_p \pm 1/3\ (001)_p^*$ appear in the SAED pattern along the $[1{-}10]_p$ zone axis but only the $G_p \pm 1/3\ (001)_p^*$ in the $[110]_p$ one. Therefore, a $\sqrt{2}a_p \times \sqrt{2}b_p \times 3c_p$ unit cell is concluded by construction of the reciprocal lattice from the SAED patterns of the $Gd_{1.2}Ba_{1.2}Ca_{0.6}Fe_3O_8$ oxide. Figure 1d shows the HRTEM image along the $[1{-}10]_p$ zone axis. Contrast differences, characteristic of the $3a_p$ periodicity along the $[001]_p$ direction, are observed in the whole crystal without domains with different crystal microstructures. All crystals studied present long-range modulation in their crystal structure.

HAADF-STEM images (Z contrast images) in combination with EELS mapping give information about the cation

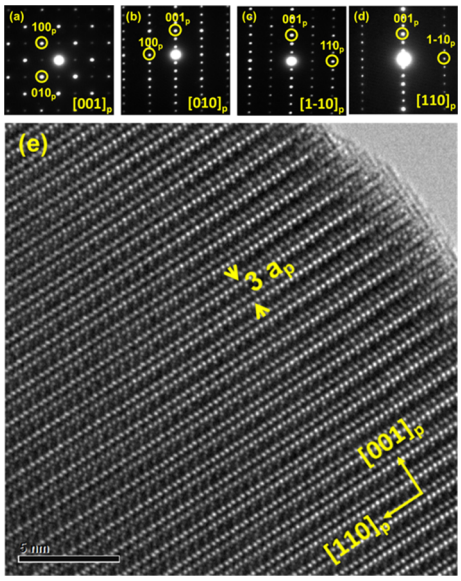

Figure 1. Experimental SAED patterns of a crystal of $Gd_{1.2}Ba_{1.2}Ca_{0.6}Fe_3O_8$ along the (a) $[001]_p$, (b) $[010]_p$, (c) $[1{-}10]_p$, and (d) $[110]_p$ zone axes. The patterns have been indexed on the basis of a cubic perovskite structure. (d) Experimental HRTEM image of the crystal along the $[1{-}10]_p$ zone axis.

arrangement within the structure with atomic resolution, which, in addition to the information provided by SAED and HRTEM, allows to solve the crystal structure of the compound. Figure 2a,b shows the HAADF-STEM images along the $[010]_p$ and $[1{-}10]_p$ zone axes of a crystal of $RE_{1.2}Ba_{1.2}Ca_{0.6}Fe_3O_8$.

The contrast differences in the images confirm the $3a_p$ superstructure along the $[001]_p$ direction as due to A-cation ordering. The EELS mapping (Figure 2d) reveals the layered-type ordering of the A-cations as a sequence of two consecutive layers containing both Gd and Ca atoms alternated with one layer of Ba atoms (i.e., Gd/Ca−Gd/Ca−Ba−Gd/Ca sequence). In addition to the contrast associated with the layered ordering of the A-cations, the layers of columns of Fe atoms located between the two layers of columns containing Gd and Ca show weaker contrast than the layers of columns of Fe atoms located between one layer of columns of Ba atoms and one containing Gd and Ca.

This weaker contrast seems to be associated with a lower anion coordination of the Fe atoms in those positions. Moreover, the image of the $[-110]_p$ zone axis reveals that these Fe-layers present two clearly different Fe−Fe distances (0.34 and 0.24 nm) alternating along the $[110]_p$ direction (indicated in the figure by yellow and red frames). In order to visualize the anion sublattice, ABF−STEM experiments were carried out. Figure 3 shows the ABF−STEM image of a crystal of the compound along the $[-110]_p$ zone axis. Both the ABF−STEM image and the corresponding HAADF-STEM image along the $[-110]_p$ zone axis are also shown in Supporting Information, Figure S3 for comparison. The columns of oxygen atoms are indicated in yellow. Two different oxygen environments around the Fe cations are clearly distinguished: the diffuse contrast associated with the oxygen atoms in the Fe−O layer between layers containing Gd and Ca indicates a low, probably, four-oxygen coordination of Fe (Fe in the oxygen-tetrahedral polyhedron); in the other two Fe−O layers of the unit cell, the two columns of oxygen atoms beside the Fe-atom

DOI: 10.1021/acs.chemmater.9b02716
Chem. Mater. 2019, 31, 5993−6000

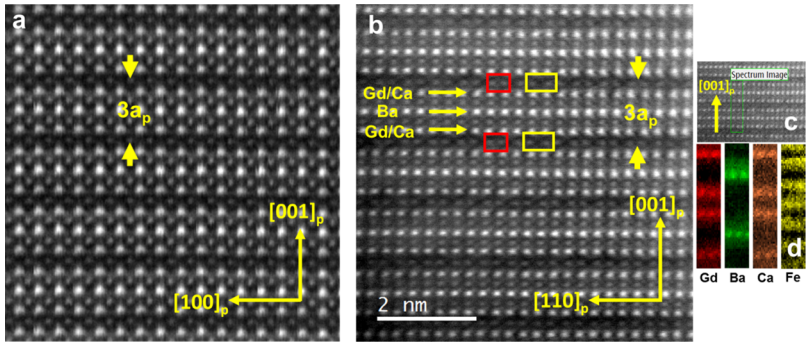

Figure 2. Experimental HAADF-STEM images of a crystal of $Gd_{1.2}Ba_{1.2}Ca_{0.6}Fe_3O_8$ along the (a) $[010]_p$ and (b,c) $[1{-}10]_p$ zone axes and (d) EELS maps of the area of the crystal indicated in green in (c). Columns of Gd atoms are indicated in red, Ba atoms in green, Ca atoms in brown, and Fe atoms in yellow. Two Fe−Fe distances (0.34 and 0.24 nm) along the $[110]_p$ direction are indicated with yellow and red frames, respectively.

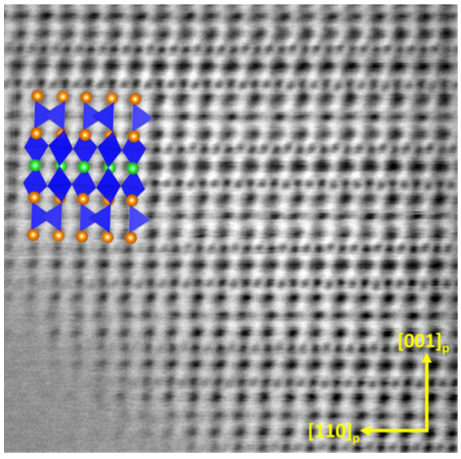

Figure 3. Experimental ABF−STEM image of a crystal of $Gd_{1.2}Ba_{1.2}Ca_{0.6}Fe_3O_8$ along the $[1{-}10]_p$ zone axis. Green spheres mark columns of Ba atoms, orange spheres mark columns of Gd/Ca atoms, and coordination polyhedra around Fe atoms are indicated in blue.

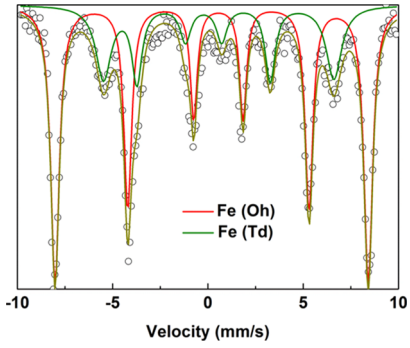

Figure 4. Mössbauer spectra of $Gd_{1.2}Ba_{1.2}Ca_{0.6}Fe_3O_8$ at room temperature. The dots show experimental data, and the lines show the Lorentzian fits. Red line marks the peaks for Fe in octahedral sites, and the green line marks the peaks for Fe in tetrahedral sites.

columns are clearly viewed, indicating Fe located in octahedral coordination. The stacking sequence along the $[001]_p$ direction of the Fe-coordination polyhedra results in a tetrahedra−octahedra−octahedra−tetrahedra (T−O−O−T) ordering. The image also reveals a slight tilting of the oxygen-octahedra as a consequence of shifting of the oxygen atoms of the Fe−O layers toward the Gd/Ca−O layers.

In summary, the TEM analyses conclude that the $Gd_{1.2}Ba_{1.2}Ca_{0.6}Fe_3O_8$ oxide presents a layered-type perovskite structure with a $\sqrt{2}\,a_p \times \sqrt{2}\,b_p \times 3c_p$ unit cell related to the layered ordering of A-cations in a Gd/Ca-Gd/Ca-Ba-Gd/Ca sequence with a combined T−O−O−T ordering sequence of the Fe−O polyhedra. Lower magnification images of different crystals clearly show a long-range formation of this perovskite superstructure.

Mössbauer analysis performed at room temperature (Figure 4) reveals a complex spectrum that consists of two different components in an area ratio 2:1 with ISs of 0.37 and 0.17 mm/s, and quadrapolar splittings (QSs) of −0.36 and 0.79 mm/s, respectively. These different ISs and QSs are attributed to the two different Fe^{3+} sites (in octahedral and tetrahedral coordination) as determined by structural analysis, consistent with the Mössbauer area ratio. Moreover, both Fe components are split into six lines, indicating magnetic ordering of the Fe within the crystal structure with hyperfine parameters (HF) of 50 and 37 T for octahedral and tetrahedral sites, respectively.

With the aim of refining the crystal structure concluded from the SAED, HRTEM, and STEM results, SXRD measurements at room temperature were performed. The space group was determined from the following reflection extinctions $0kl$: $k = 2n + 1$ and $0k0$: $k = 2n + 1$, which have been deduced by the construction of the reciprocal lattice from the SAED patterns (the pattern of the $[001]_p$ zone axis shows double diffraction, which disappears by tilting the crystal along the direction containing the forbidden reflections, as shown in Supporting Information, Figure S4). These reflection extinctions correspond to the extinction *Pb*-- group, which allows the space groups $Pb2_1m$, *Pbm*2, and *Pbmm*. The space groups, *Pbm*2 and *Pbmm*, can be discarded because give a multiplicity of the sites that needs the splitting of the position of some atoms in the structural model inferred by STEM analyses. Therefore, $Pb2_1m$ is the space group of the crystal structure of this compound. This space group and unit cell are in agreement with the threefold perovskite superstructures found in other Fe-oxides.[23,27] $Pb2_1m$ lacks inversion center leading to a possible polarization along the *b*-direction. Results of the crystal structure refinement (Supporting Information, Figure S5 and Table S1) confirm the deduced $\sqrt{2}\,a_p \times \sqrt{2}\,b_p \times 3c_p$ unit cell with the orthorhombic $Pb2_1m$ space group and the threefold layered ordering of the Gd, Ba, and Ca atoms. Despite the EELS mapping of $Gd_{1.2}Ba_{1.2}Ca_{0.6}Fe_3O_8$ which concludes that the Ba atoms are located in a single (001)-layer, the composition of this oxide, in agreement with the nominal

DOI: 10.1021/acs.chemmater.9b02716
Chem. Mater. 2019, 31, 5993−6000

one according to the XEDS results, indicates that a small concentration of Ba atoms should be located within the Gd/Ca layers. In fact, in the refinement of the crystal structure, 10% of Ba atoms in the 4c crystallographic positions have been considered.

Recalling that $Gd_{0.8}Ba_{0.8}Ca_{0.4}Fe_2O_{5.33}$ ($Gd_{1.2}Ba_{1.2}Ca_{0.6}Fe_3O_8$) represents one end member of the solid solution $Gd_{0.8}Ba_{0.8}Ca_{0.4}Co_{2-x}Fe_xO_{5+\delta}$, the above detailed structural analysis permits to make a first remark concerning the change from a $10a_p$ to $3a_p$ perovskite superstructure, as Co is completely substituted by Fe while maintaining the Gd, Ba, Ca ratio.[28] This structural change is probably related to the suppression of the isolated Gd−O layers, which are present in the case of $Gd_{0.8}Ba_{0.8}Ca_{0.4}Co_{1.6}Fe_{0.4}O_{5.41}$. These Gd−O layers concentrate the oxygen vacancies, avoiding the formation of the tetrahedral anion environments around the Fe/Co cations. In $Gd_{0.8}Ba_{0.8}Ca_{0.4}Co_{1.6}Fe_{0.4}O_{5.41}$, the stacking sequence of the different A−O layers (Gd/Ca-Gd/Ca-Ba-Gd-Ba-Gd/Ca) contains one isolated Gd−O layer resulting in a $5a_p$ periodicity. To accommodate the oxygen content and taking into account that the Gd−O planes stabilize the location of anion vacancies, the stacking sequence of the coordination polyhedra around the Co/Fe atoms is T−O−O_v−O_v−O−T (O_v denotes oxygen-octahedra containing oxygen vacancies located within the Gd−O layers) along the same direction as the layered A-cation ordering (the different orientation of the two consecutive T-layers originates the $10a_p$ periodicity). The greater capability of the Fe cations compared to the Co ones to be surrounded by tetrahedral anion polyhedra might be the reason for increasing the number of T-layers per unit cell, leading to the stoichiometric $Gd_{1.2}Ba_{1.2}Ca_{0.6}Fe_3O_8$ and also for driving a different ordering sequence in the A-cation sublattice, without isolated Gd−O layers that could capture anion vacancies. A further interesting structural feature found in $Gd_{1.2}Ba_{1.2}Ca_{0.6}Fe_3O_8$ is the singular stacking sequence of the A-cations. Two other Fe oxides with the general formula $YBa_2Fe_3O_8$[29] and $LaCa_2Fe_3O_8$[23] and with a $3a_p$ superstructure have been previously reported. These oxides present AE^{2+}−AE^{2+}−RE^{3+}−AE^{2+} (AE: alkaline earth and RE: rare earth) ordering giving the same threefold modulation, but the Fe coordination sequence differs in these two compounds. While in $YBa_2Fe_3O_8$, the Y^{3+} layers create two square-based pyramidal polyhedra around Fe (O−SP−SP−O stacking sequence), $LaCa_2Fe_3O_8$ presents only one Fe-layer in the tetrahedral environment in between the two consecutive Ca^{2+} layers (T−O−O−T stacking sequence), like in $Gd_{1.2}Ba_{1.2}Ca_{0.6}Fe_3O_8$. However, $LaCa_2Fe_3O_8$ and $Gd_{1.2}Ba_{1.2}Ca_{0.6}Fe_3O_8$ differ in the cation distribution within the A-sublattice.

Therefore, $Gd_{1.2}Ba_{1.2}Ca_{0.6}Fe_3O_8$ presents a novel stacking sequence of the A-cations where the RE^{3+} layers are adjacent to the T layers.

The cell parameters of $Gd_{1.2}Ba_{1.2}Ca_{0.6}Fe_3O_8$ undergo a nonisotropic linear expansion upon heating without showing any discontinuity according to the Le-Bail fitting of the SXRD patterns up to 1000 K (Supporting Information, Figure S6). The linear expansion of the unit cell suggests a fixed oxygen content from room temperature to 1000 K, as confirmed by TGA in air, which shows no weight variations outside of the error range of measurement (Supporting Information, Figure S7).

Polar Properties. The polar space group $Pb2_1m$ of the $Gd_{1.2}Ba_{1.2}Ca_{0.6}Fe_3O_8$ oxide admits the existence of a net polarization from uncompensated shifts of the cations within the structure.

The polarization P can be calculated from the Rietveld refinement results using the following equation

$$P = \frac{C}{\Omega}\sum_i q_i r$$

where C is the Coulomb constant, Ω is the unit cell volume, q_i is the charge of the i cation, and r_i is the shifting of the i cation with respect to the theoretical centrosymmetric structure. Each ion has been treated as a point charge when calculating the polarization.

The alternating Ba and Gd/Ca layers exhibit antipolar displacements from their ideal positions along the c-axis. The displacement of the Ba atoms is lower than those of the Gd and Ca atoms, resulting, in principle, in a total polarization, as shown in Figure 5a. However, the presence of the mirror plane

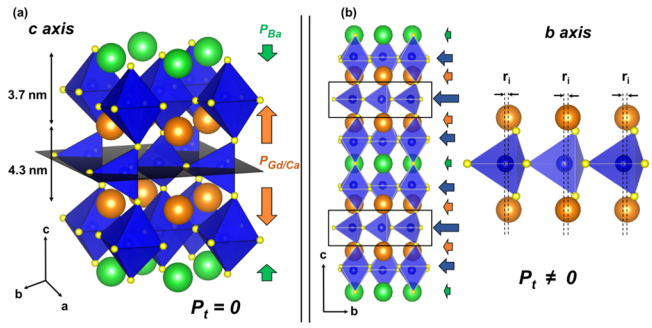

Figure 5. Graphic representation of the polar unit cell of $Gd_{1.2}Ba_{1.2}Ca_{0.6}Fe_3O_8$. (a) Arrows indicate polarization due to Ba atoms (green) and Gd/Ca atoms (orange) displacements along the c-axis. The length of the arrows is proportional to P. The m plane perpendicular to the c-axis (represented in gray) cancels out P_t. (b) Arrows indicate polarization in the different layers (Ba−O layers in green, Gd/Ca−O in orange, Fe−O in octahedral layers, and Fe−O in tetrahedral layers), including the anionic and cationic contributions along the b-axis. r_i is the shift distance of the Fe atoms with respect to the A-cations along the b-axis.

m perpendicular to the c-axis cancels out this polarization, contrary to the situation observed in the epitaxially grown $SrFeO_{2.5}/CaFeO_{2.5}$ thin-film superlattices.[20]

On the contrary, all tetrahedrally coordinated Fe atoms are shifted in the same direction along the b-axis, creating polarization, as shown in Figure 5b. The polar space group $Pb2_1m$ allows the tetrahedral layers to have the same handedness (left-handed in the Figure 5) within the entire structure, creating an in-plane polarization. Besides, not only the Fe cations in a tetrahedral environment but all atoms within the structure are shifted from their theoretical positions in the nondistorted structure, contributing to the net polarization. Taking into account both the anion and cation shifts and assuming the middle point of the distance between consecutive Ba cations in the layer as the reference point for calculating the shifts of the atoms, the resulting polarization is 33.0 $\mu C/cm^2$ along the b-axis (note that the polarization has been calculated from the SXRD results, which do not give precise values of the oxygen coordinates).

Magnetic and Electron-Transport Properties. The room temperature M−H variation (Supporting Information, Figure S8) is linear up to 5 T and has no remanence or coercivity, suggesting an AFM-type ordering of Fe^{3+} (d^5, HS, S

DOI: 10.1021/acs.chemmater.9b02716
Chem. Mater. 2019, 31, 5993−6000

= 5/2) within the structure. The temperature dependence of the magnetic susceptibility under a magnetic field of 5 Oe in the range between 300 and 1000 K, shown in Figure 6a, sets the AFM ordering temperature well above the room temperature.

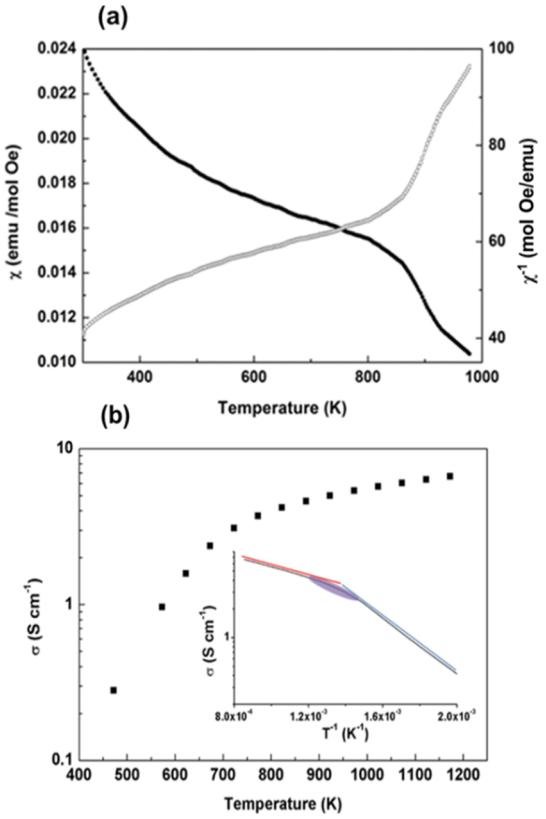

Figure 6. (a) Temperature dependence of the magnetic susceptibility of $Gd_{1.2}Ba_{1.2}Ca_{0.6}Fe_3O_8$ within the range 300−1000 K. (b) Total dc conductivity as a function of temperature of $Gd_{1.2}Ba_{1.2}Ca_{0.6}Fe_3O_8$. The inset depicts the Arrhenius dependence of conductivity with temperature, with the two different regimes shown in red and blue. The purple zone indicates the extension of the intermediate region.

The inverse of the magnetic susceptibility deviates from the linearity at T = 850 K, indicating magnetic ordering of Fe below this temperature without any change in the oxidation state of Fe according to the TGA.

Besides, the variation of the electrical resistance of the oxide as a function of temperature (Figure 6b) reveals two linear trends between 450 and 1200 K with a change in the slope, which should be associated with the magnetic ordering. This change cannot be related to a modification in the oxidation state of Fe because, according to the TGA, the oxygen content remains constant in this temperature regime. A semiconducting behavior is observed over the whole range of temperatures with two different regimes below ∼700 K and above ∼890 K with activation energies E_a = 288 and 112 meV, respectively.

It seems that there is not an electrical transition at a particular temperature, but the change of regime takes place in a range of 150 K, which evidences some anomalies in the magnetic behavior of this compound (the magnetic transition occurs at about 850 K). This close relation between electronic conductivity and magnetic behavior is observed in other Fe^{3+}-containing compounds such as $Ca_2Fe_2O_5$[30] and $NdFeO_3$,[31] in which the spin alignment via superexchange (Fe^{3+}−O^{2-}−Fe^{3+}) localizes the electrons, increasing the electrical E_a.

Magnetic Structure. NPD patterns collected between 300 and 1000 K were used to determine the magnetic structure of the compound replacing Tb^{3+} by Gd^{3+} because of the high absorption of this latter cation. The replacement of Gd by Tb maintains the nuclear structure according to the NPD data refinement (Table 1 in the main text and in Supporting Information, Table S2) and the AFM ordering, although the paramagnetic behavior differs probably due to the different contribution of Tb^{3+} to the total magnetic moment (Supporting Information, Figure S9). Tb-oxide also presents a polar moment of 23.2 $\mu C/cm^2$ along the b-axis. Magnetic reflections in the NPD patterns of $Tb_{1.2}Ba_{1.2}Ca_{0.6}Fe_3O_8$ appear below 700 K. The magnetic reflections can be indexed by a propagation vector [0 0 1/2], as shown in Figure 7a, producing a magnetic unit cell $\sqrt{2}\,a_p \times \sqrt{2}\,b_p \times 6c_p$. Magnetic symmetry analysis was used to determine the allowed irreducible representations and their basis vectors for the Fe^{3+}-site and are included in Supporting Information, Table S3. The magnetic structure adopted below 700 K is presented in Figure 8. It consists of a three-dimensional G-type antiferromagnetically ordered arrangement of the Fe spins, with the spin directions lying along the b-axis. At room temperature, two different magnetic moments of 4.04(9) μ_B and 3.1(2) μ_B for Fe in octahedral and tetrahedral sites, respectively, are determined, both lower than the theoretical value of 5 μ_B. This fact can be explained by the lowering of the magnetic moment associated with the thermal spin fluctuations. As shown in

Table 1. Results of the Rietveld Refinement of the Crystal Structure of $Tb_{0.8}Ba_{0.8}Ca_{0.4}Fe_2O_{5.33}$ from NPD Data at Room Temperature[a]

atom	site	x	y	Z	B_{iso}	occupancy
Ba	2a	0.265(2)	0.75	0.0	0.9(1)	1
Tb/Ca/Ba	4c	0.261(1)	0.743(1)	0.3154(4)	1.07(8)	0.548(2)/0.350(2)/0.103(2)
Fe (Oh)	4c	0.2467(9)	0.246(3)	0.1692(2)	0.86(4)	1
Fe (Td)	2b	0.2072(9)	0.224(3)	0.5	0.86(4)	1
O1	4c	0.001(3)	0.003(3)	0.2001(4)	0.98(4)	1
O2	4c	0.499(3)	0.011(4)	0.1731(5)	0.98(4)	1
O3	2b	0.129(2)	0.859(4)	0.5000	0.98(4)	1
O4	2a	0.234(2)	0.262(4)	0.0	0.98(4)	1
O5	4c	0.307(1)	0.280(4)	0.3572(3)	0.98(4)	1

[a]The y position of Ba has been fixed since it has been taken as the reference point for calculating the polarization of the cell. [b]a = 5.5721(1), b = 5.5173(1), c = 11.5786(3), R_{wp} = 4.69%, R_p = 3.59%, R_{exp} = 1.76%, R_B = 6.66%, and χ^2 = 7.12.

DOI: 10.1021/acs.chemmater.9b02716
Chem. Mater. 2019, 31, 5993−6000

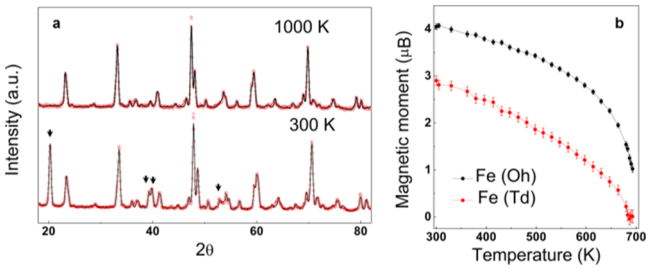

Figure 7. (a) PND patterns of $Tb_{1.2}Ba_{1.2}Ca_{0.6}Fe_3O_8$ taken below (300 K) and above (1000 K) the magnetic transition. The arrows indicate the magnetic reflections. (b) Temperature dependence of the magnetic moment of Fe in the octahedral (black) and tetrahedral (red) sites of $Tb_{1.2}Ba_{1.2}Ca_{0.6}Fe_3O_8$.

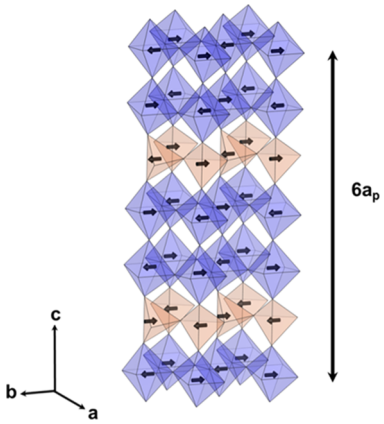

Figure 8. Magnetic unit cell of $Tb_{1.2}Ba_{1.2}Ca_{0.6}Fe_3O_8$. Arrows indicate the spin direction.

Figure 7b, the magnetic moment of Fe in both sites follows a characteristic Brillouin curve. Moreover, the lower magnetic moment can furthermore be associated with a non-pure ionic bonding between Fe and O. The covalence degree, more marked in the tetrahedral sites, induces the transfer of some magnetic moment to the O atoms, decreasing the magnetic moment.

The long-range AFM structure extends up to ~690 K. Above this temperature, short-range magnetic order is still visible up to about 800 K in the neutron diffraction data of D20 as a broad contribution. This short-range ordering mirrors the presence of magnetic interactions of Fe up to ~850 K according to the magnetic measurements, as already found in Ca_2FeMnO_5.[32]

CONCLUSIONS

In conclusion, room-temperature multiferroism in polycrystalline AFM Fe perovskites is reported for the first time. These perovskite-type oxides with composition $RE_{1.2}Ba_{1.2}Ca_{0.6}Fe_3O_8$ (RE = Gd, Tb) have been prepared by the ceramic method. The interplay of layered ordering of the Gd(Tb), Ba, and Ca atoms with the ordering of the FeO_4-tetrahedra (T) and FeO_6-octahedra (O) results in a orthorhombic polar crystal structure with a non-centrosymmetric $Pb2_1m$ space group. The layered structure consists of the stacking sequence of RE/Ca-RE/Ca-Ba-RE/Ca layers in combination with TOOT layers in a $\sqrt{2}a_p \times \sqrt{2}b_p \times 3c_p$ unit cell. A polar moment of 33.0 $\mu C/cm^2$ for the Gd-oxide (23, 2 $\mu C/cm^2$ for the Tb one) is determined from the displacements of the cations, mainly Fe, and oxygen atoms along the *b*-axis. These oxides present AFM ordering in a $\sqrt{2}a_p \times \sqrt{2}b_p \times 6c_p$ magnetic unit cell, determined in the Tb compound. AFM ordering is maintained up to 690 K, which is one of the highest transition temperatures reported in Fe perovskites. The magnetic transition is associated with an electric transition of electron transport at the same temperature. Although these results open new perspectives to multifunctionality in perovskites, the magnetoelectric coupling of the ferroic properties would be essential for some applications. In this sense, studies of electric field control of magnetism or electric polarization under magnetic fields are interesting to be carried out in these Fe perovskites.

ASSOCIATED CONTENT

Supporting Information

The Supporting Information is available free of charge on the ACS Publications website at DOI: 10.1021/acs.chemmater.9b02716.

PXRD patterns, EELS spectrum, HAADF-STEM and ABF−STEM images, SAED patterns, refined crystal structure parameters, lattice parameters versus *T*, TGA, *M* versus *H*, χ and χ^{-1} versus *T*, and irreducible representations and basis vectors of Fe in the magnetic structure (PDF)

AUTHOR INFORMATION

Corresponding Author

*E-mail: sgmartin@ucm.es. Phone: (+34) 91 394 4214.

ORCID

Masato Goto: 0000-0002-8198-7622
Ulises Amador: 0000-0002-4412-2419
Yuichi Shimakawa: 0000-0003-1019-2512
Susana García-Martín: 0000-0003-0729-4892

Notes

The authors declare no competing financial interest.

ACKNOWLEDGMENTS

This work has been supported by the Spanish MINECO through projects MAT2016-78362-C4-1-R and MAT2016-78362-C4-4-R and the Japan Society for the Promotion of Science (JSPS) for Grants-in-Aid for Scientific Research (no. 16H02266) and the Core-to-Core Program (A) Advanced Research Networks. We thank ILL for the financial support and for beam time allocation, experiment code 5-21-1116, doi:105291/ILL-DATA.5-21-1116. X.M.d.I.-L. thank the MECD for the grant FPU014/05971. We thank Prof. Miguel A. Alario Franco, Prof. Takashi Saito, and Prof. Fabio Denis Romero for discussion. We thank Syogo Kawaguchi for assistance with the SXRD experiments at SPring-8 and Wei-Tin Chen, Yu-Chun Chuang, and Hwo-Shuenn Sheu for help with the SXRD experiments at TPS in NSRRC. We also thank Dr. Daniel Muñoz for helping with dc-electrical conductivity measurements and Dr. Alicia Palencia for helping in magnetic measurements. We acknowledge the Microscopy Centre of the UCM for providing facilities.

REFERENCES

(1) Tilley, R. J. D. Perovskites: Structure−Property Relationships. *MRS Bull.* **2017**, *42*, 325 DOI: 10.1557/mrs.2017.81.

DOI: 10.1021/acs.chemmater.9b02716
Chem. Mater. 2019, 31, 5993−6000

(2) Glazer, A. M.; IUCr. The Classification of Tilted Octahedra in Perovskites. *Acta Crystallogr. Sect. B Struct. Crystallogr. Cryst. Chem.* **1972**, *28*, 3384−3392.
(3) Glazer, A. M. Simple Ways of Determining Perovskite Structures. *Acta Crystallogr., Sect. A* **1975**, *31*, 756−762.
(4) Woodward, P. M. Octahedral Tilting in Perovskites. I. Geometrical Considerations. *Acta Crystallogr. Sect. B Struct. Sci.* **1997**, *53*, 32−43.
(5) Imada, M.; Fujimori, A.; Tokura, Y. Metal-Insulator Transitions. *Rev. Mod. Phys.* **1998**, *70*, 1039−1263.
(6) King, G.; Woodward, P. M. Cation Ordering in Perovskites. *J. Mater. Chem.* **2010**, *20*, 5785.
(7) Trukhanov, S. V.; Troyanchuk, I. O.; Hervieu, M.; Szymczak, H.; Bärner, K. Magnetic and Electrical Properties of $LBaMn_2O_{6-\gamma}$ (L = Pr , Nd, Sm, Eu, Gd, Tb) Manganites. *Phys. Rev. B* **2002**, *66*, 184424.
(8) Ueda, Y.; Nakajima, T. Novel Structures and Electromagnetic Properties of the A-Site-Ordered/Disordered Manganites $RBaMn_2O_6$ /$R_{0.5}Ba_{0.5}$ MnO_3 (R = Y and Rare Earth Elements). *J. Phys. Condens. Matter* **2004**, *16*, S573−S583.
(9) Marezio, M. Oxygen Stoichiometry in High-Tc Superconductors. *Acta Crystallogr., Sect. A: Found. Crystallogr.* **1991**, *47*, 640−654.
(10) Taskin, A. A.; Lavrov, A. N.; Ando, Y. Achieving Fast Oxygen Diffusion in Perovskites by Cation Ordering. *Appl. Phys. Lett.* **2005**, *86*, 091910.
(11) Ávila-Brande, D.; King, G.; Urones-Garrote, E.; Subakti; Llobet, A.; García-Martín, S. Structural Determination and Imaging of Charge Ordering and Oxygen Vacancies of the Multifunctional Oxides $REBaMn_2O_{6-\chi}$ (RE = Gd, Tb). *Adv. Funct. Mater.* **2014**, *24*, 2510−2517.
(12) King, G.; Llobet, A.; Garcia-Martin, S. Magnetic Properties and Magnetic Structures of $TbBaMn_2O_{5.75}$: Possible Observation of Unconventional Polaron Trimers. *Phys. Rev. B: Condens. Matter Mater. Phys.* **2015**, *91*, 024412.
(13) Spaldin, N. A.; Ramesh, R. Advances in Magnetoelectric Multiferroics. *Nat. Mater.* **2019**, *18*, 203−212.
(14) Hill, N. A. Why Are There so Few Magnetic Ferroelectrics? *J. Phys. Chem. B* **2000**, *104*, 6694−6709.
(15) Khomskii, D. I. Multiferroics: Different Ways to Combine Magnetism and Ferroelectricity. *J. Magn. Magn. Mater.* **2006**, *306*, 1−8.
(16) Rondinelli, J. M.; Eidelson, A. S.; Spaldin, N. A. Non-d^0 Mn-Driven Ferroelectricity in Antiferromagnetic $BaMnO_3$. *Phys. Rev. B: Condens. Matter Mater. Phys.* **2009**, *79*, 205119.
(17) Hartman, S. T.; Cho, S. B.; Mishra, R. Multiferroism in Iron-Based Oxyfluoride Perovskites. *Inorg. Chem.* **2018**, *57*, 10616−10624.
(18) Young, J.; Lalkiya, P.; Rondinelli, J. M. Design of Non-centrosymmetric Perovskites from Centric and Acentric Basic Building Units. *J. Mater. Chem. C* **2016**, *4*, 4016−4027.
(19) Rondinelli, J. M.; Fennie, C. J. Octahedral Rotation-Induced Ferroelectricity in Cation Ordered Perovskites. *Adv. Mater.* **2012**, *24*, 1961−1968.
(20) Young, J.; Moon, E. J.; Mukherjee, D.; Stone, G.; Gopalan, V.; Alem, N.; May, S. J.; Rondinelli, J. M. Polar Oxides without Inversion Symmetry through Vacancy and Chemical Order. *J. Am. Chem. Soc.* **2017**, *139*, 2833−2841.
(21) Woodward, P. M.; Karen, P. Mixed Valence in $YBaFe_2O_5$. *Inorg. Chem.* **2003**, *42*, 1121.
(22) Shang, M.; Zhang, C.; Zhang, T.; Yuan, L.; Ge, L.; Yuan, H.; Feng, S. The Multiferroic Perovskite $YFeO_3$. *Appl. Phys. Lett.* **2013**, *102*, 062903.
(23) Hudspeth, J. M.; Goossens, D. J.; Studer, A. J.; Withers, R. L.; Norén, L. The Crystal and Magnetic Structures of $LaCa_2Fe_3O_8$ and $NdCa_2Fe_3O_8$. *J. Phys. Condens. Matter* **2009**, *21*, 124206.
(24) Rodriguez-carvajal, J. Structural Analysis from Powder Diffraction Data The Rietveld Method. *Ec. Themat. Cristallogr. neutrons* **1997**, *418*, 73−95.
(25) Rodríguez-Carvajal, J. *BasIreps A Program for Calculating Irreducible Representation of Little Groups and Basis Functions of Polar and Axial Vector Properties*. (**2010**) Fullprof Suite (ILL).
(26) Ritter, C. Neutrons Not Entitled to Retire at the Age of 60: More than Ever Needed to Reveal Magnetic Structures. *Solid State Phenom.* **2011**, *170*, 263−269.
(27) Allix, M.; Battle, P. D.; Frampton, P. P. C.; Rosseinsky, M. J.; Ruiz-Bustos, R. Composition Dependence of the Structural Chemistry and Magnetism of $Ca_{2.5}Sr_{0.5}(Ga,Co)_{1+x}Mn_{2-x}O_8$. *J. Solid State Chem.* **2006**, *179*, 775−792.
(28) de Irujo-Labalde, X. M.; Muñoz-Gil, D.; Urones-Garrote, E.; Ávila-Brande, D.; García-Martín, S. Complex Modulation of the Crystal Structure of a Layered Perovskite. A Promising Solid-Oxide-Fuel-Cell Cathode. *J. Mater. Chem. A* **2016**, *4*, 10241−10247.
(29) Karen, P.; Suard, E.; Fauth, F. Crystal Structure of Stoichiometric $YBa_2Fe_3O_8$. *Inorg. Chem.* **2005**, *44*, 8170.
(30) Shaula, A.; Pivak, Y.; Waerenborgh, J.; Gaczynski, P.; Yaremchenko, A.; Kharton, V. Ionic Conductivity of Brownmillerite-Type Calcium Ferrite under Oxidizing Conditions. *Solid State Ionics* **2006**, *177*, 2923−2930.
(31) Yo, C. H.; Jung, I. Y.; Ryu, K. H.; Ryu, K. S.; Choy, J. H. A Study of the Nonstoichiometry and Physical-Properties of the Perovskite $Nd_{1-X}Ca_xFeo_{3-Y}$ System. *J. Solid State Chem.* **1995**, *114*, 265−270.
(32) Ramezanipour, F.; Cowie, B.; Derakhshan, S.; Greedan, J. E.; Cranswick, L. M. D. Crystal and Magnetic Structures of the Brownmillerite Compound $Ca2Fe_{1.039(8)}Mn0_{.962(8)})O_5$. *J. Solid State Chem.* **2009**, *182*, 153−159.

DOI: 10.1021/acs.chemmater.9b02716
Chem. Mater. 2019, 31, 5993−6000